Physics and Chemistry of Minerals (2018) 45:759–772
https://doi.org/10.1007/s00269-018-0960-3

ORIGINAL PAPER

Fe–Mg substitution in aluminate spinels: effects on elastic properties investigated by Brillouin scattering

Enrico Bruschini[1,2] · Sergio Speziale[2] · Ferdinando Bosi[1] · Giovanni B. Andreozzi[1]

Received: 27 November 2017 / Accepted: 9 March 2018 / Published online: 22 March 2018

Abstract

We investigated by a multi-analytical approach (Brillouin scattering, X-ray diffraction and electron microprobe) the dependence of the elastic properties on the chemical composition of six spinels in the series $(Mg_{1-x},Fe_x)Al_2O_4$ ($0 \le x \le 0.5$). With the exception of C_{12}, all the elastic moduli (C_{11}, C_{44}, K_{S0} and G) are insensitive to chemical composition for low iron concentration, while they decrease linearly for higher Fe^{2+} content. Only C_{12} shows a continuous linear increase with increasing Fe^{2+} across the whole compositional range under investigation. The high cation disorder showed by the sample with $x = 0.202$ has little or no influence on the elastic parameters. The range $0.202 < x < 0.388$ bounds the percolation threshold (p_c) for nearest neighbor interaction of Fe in the cation sublattices of the spinel structure. Below $x = 0.202$, the iron atoms are diluted in the system and far from each other, and the elastic moduli are nearly constant. Above $x = 0.388$, Fe atoms form extended interconnected clusters and show a cooperative behavior thus affecting the single-crystal elastic moduli. The elastic anisotropy largely increases with the introduction of Fe^{2+} in substitution of magnesium in spinel. This behavior is different with respect to other spinels containing transition metals such as Mn^{2+} and Co^{2+}.

Keywords Mg–Fe^{2+} substitution · Spinels · Elasticity · Brillouin scattering · Crystal chemistry · Percolation threshold · Elastic anisotropy

Introduction

Knowing the elastic properties of minerals is of crucial importance in geosciences for the correct interpretation of seismological data (e.g., Birch 1952; Jackson 1983; Brown and McQueen 1986; Duffy et al. 1995; Li and Liebermann 2007; Bass et al. 2008). Since both pressure and temperature increase as a function of depth, much experimental and theoretical work has been done to understand how these two variables affect the physical properties of minerals (e.g., Karki et al. 1997; Steinle-Neumann et al. 2001; Speziale et al. 2004; Murakami et al. 2012; Lu et al. 2013; Yang et al. 2014; Mao et al. 2015; Pamato et al. 2016; Zhang and Bass 2016; Duan et al. 2018).

Most of the minerals relevant to geophysics (e.g., olivine, spinel, garnet, magnesiowüstite) are solid solutions between two (or more) endmember compositions; therefore, an in-depth understanding of the relationships between their chemical composition and physical properties is of great relevance. Experimental results obtained at high pressure and high temperatures can be well described and modeled according to widely accepted thermodynamic approaches (eulerian finite strain, thermal equation of state; e.g., Birch 1938, 1947; Davies and Dziewonski 1975; Jackson and Rigden 1996; Angel 2000; Li and Zhang 2005; Stixrude and Lithgow-Bertelloni 2005). On the opposite, the influence of chemical composition on elasticity is not yet fully understood (sometimes it is even ambiguous), and overall it is not satisfactorily modeled by a well-defined theoretical approach. Many extant studies have tried to tackle the problem of understanding how chemical substitutions and their effects on structural properties influence the elasticity of solid solutions, (e.g., Slagle and McKinstry 1967;

Electronic supplementary material The online version of this article (https://doi.org/10.1007/s00269-018-0960-3) contains supplementary material, which is available to authorized users.

✉ Giovanni B. Andreozzi
gianni.andreozzi@uniroma1.it

[1] Department of Earth Sciences, Sapienza University of Rome, Piazzale Aldo Moro 5, 00185 Rome, Italy

[2] Helmholtz Centre Potsdam-GFZ German Research Centre for Geosciences, Telegrafenberg, 14473 Potsdam, Germany

Isaak and Graham 1976; Jackson et al. 1978; Giri and Mitra 1986; Tatli and Özkan 1987; Angel et al. 1988; Duffy and Vaughan 1988; Zhang and Reeder 1999; Reichmann et al. 2000; Jacobsen et al. 2002; Angel 2004; Jiang et al. 2004; Speziale et al. 2004; Nestola et al. 2006; Marquardt et al. 2009; Pamato et al. 2016; Buchen et al. 2017; Kurnosov et al. 2017). However, some review studies discuss samples with different origin, thermobaric history or synthesis methods, thus lacking internal consistency. Furthermore, most of these works are limited to either natural samples of complex chemical compositions or to synthetic endmember compositions.

Recently, Reichmann and Jacobsen (2006) and Riechmann et al. (2013) explored the systematic relations between crystal chemistry and elastic properties of oxides and silicates with spinel structure, and pointed out that systematic trends of density and elastic moduli of spinels with transition metals in both the octahedrally (*M*) and tetrahedrallycoordinated sites (*T*) violate the empirical Birch's law (1961), and the transition metal-rich compositions are prone to low pressure phase transitions. Transition metals (especially, Fe) are known to affect the crystal structure and elasticity in rather complex ways (e.g., Syono et al. 1971; Lin et al. 2013). Since Fe is widespread on the Earth (dominates the core and is the fourth most abundant element in the mantle; Jackson 2000), it is of interest to systematically investigate how Fe–Mg substitution influences the structural and elastic response of Earth materials. To explore such an effect, we have chosen to investigate spinels in the series $MgAl_2O_4$–$FeAl_2O_4$ (spinel–hercynite). Minerals of the spinel–hercynite solid solution series ($MgAl_2O_4$–$FeAl_2O_4$) are important accessory phases in upper mantle assemblages and relevant components in solid inclusions of diamonds (e.g., Nestola et al. 2015).

Spinel crystals belong to the cubic system (space group: $Fd\bar{3}m$). The structure of spinel can be described in terms of anion and cation sublattices (Sickafus et al. 1999). The anions in the sublattice are arranged in a pseudo-cubic close-packed lattice, being slightly shifted in the <111> directions. The oxygen fractional coordinate is usually identified by the letter *u*. When $u = 0.25$ (assuming the origin of the unit cell at the octahedral vacancy with point symmetry $\bar{3}m$), the anion sublattice is a perfect cubic close packed (ccp) lattice. The cation sublattice corresponds to the cubic $MgCu_2$ Laves phase (Galasso 2016). The overall unit cell consists of 32 oxygen atoms with 64 tetrahedral and 32 octahedral interstices, but only 24 of these interstices are occupied by cations (8 cations in tetrahedral coordination and 16 cations in octahedral coordination). The general chemical formula of spinel is AB_2X_4, where *X* represents anions and *A* and *B* are divalent and trivalent cations, respectively, and there are eight formula units in a unit cell. A very interesting feature of the spinel structure is the possibility to incorporate a wide range of chemical species by adjusting the three structural degrees of freedom: (1) cell parameter (*a*), (2) oxygen fractional coordinate (*u*) and (3) degree of inversion (*i*) (Sickafus et al. 1999). The degree of inversion *i* quantifies the fraction of the B cation in the tetrahedrally coordinated site according to the formula: ${}^{T}(A_{1-i}B_i)^{M}(A_iB_{2-i})X_4$. The two opposite configurations are: (1) $i = 0$: no *B* cations in tetrahedra (normal spinel) and (2) $i = 1$: the *T*-site is fully occupied by *B* cations (inverse spinel). Both spinels with $i = 0$ and $i = 1$ are defined as ordered. However, only few spinels are exactly normal or inverse, very often indeed the cations can be disordered among the *M* and *T* sites and hence *i* can take values between 0 and 1. The maximum disorder is reached when $i = 2/3$. Equilibration temperature has a very important effect on the inversion degree of a spinel: higher equilibration temperatures promote cation disorder (e.g., Andreozzi et al. 2000). In principle, also pressure could affect the cation distribution of a spinel, although there is not yet a general consensus on the role of pressure in modifying the degree of disorder (e.g., Hazen and Navrotsky 1996; Nestola et al. 2007). Spinels virtually offer the possibility of understanding in which way cations in different coordination environments may affect the elastic properties of binary solid solution series (Recio et al. 2001; Mori-Sánchez et al. 2003; Bruschini et al. 2015). Many papers have already dealt with the elasticity of oxides and silicates with spinel structure, but a thorough experimental investigation of the systematic effects of Fe–Mg substitution is still missing. To the best of our knowledge, the only available data on Fe-bearing aluminate spinels are given by Wang and Simmons (1972), who reported the full set of elastic parameters for a synthetic $FeAl_2O_4$ and a natural $(Mg,Fe)Al_2O_4$ spinel. Recently, Nestola et al. (2015) studied the high pressure equation of state of $FeAl_2O_4$.

In the present study, we investigate the effects of Fe^{2+}–Mg substitution on the elasticity of cubic spinels in the system $(Mg_{1-x}Fe^{2+}_x)Al_2O_4$ with $0 \le x < 0.5$. Six gem-quality synthetic crystals were studied following a multi-analytical approach including electron microprobe analysis (EMPA), single-crystal X-ray diffraction and Brillouin scattering (BS).

Experimental methods

Crystal synthesis and sample preparation

The single crystals investigated in this study were previously synthesized and described by Andreozzi et al. (2000), Andreozzi and Lucchesi (2002) and Hålenius et al. (2002). Here, it is worth remembering that all the crystals were synthesized at the very same experimental conditions to ensure a high degree of internal consistency.

Gem-quality inclusion-free crystals were selected for the crystal chemical and Brillouin scattering measurements and were manually ground into double-side polished platelets having a thickness of 40–60 μm. The starting crystals showed a well-developed octahedral shape and for this reason all the produced platelets were parallel (or very close) to {111}, with the exception of He5a which is almost parallel to {100}. Some crystals coming from the same batch of materials from which we picked up the samples from this study were already chemically and structurally characterized (Andreozzi and Lucchesi 2002; Hålenius et al. 2002). For the sake of accuracy, we repeated the chemical and crystallographic characterization on the very same samples used for the Brillouin scattering measurements.

Single-crystal structure refinement

For X-ray data collection, the six crystal fragments used for Brillouin scattering measurement were mounted on a Bruker KAPPA APEX-II diffractometer, equipped with a CCD area detector (6.2×6.2 cm^2 active detection area, 512×512 pixels) and a graphite crystal monochromator, using Mo$K\alpha$ radiation from a fine-focus sealed X-ray tube. The sample-to-detector distance was 4 cm. More than 5000 exposures per sample were collected (step = 0.2°, time/step = 10 s) covering the full reciprocal sphere with an average redundancy of about 20. Final unit cell parameters were refined using the Bruker AXS SAINT program from about 2000 recorded reflections with $I > 10\ \sigma_I$ in the range $8° < 2\theta < 90°$. The intensity data were processed and corrected for Lorentz, polarization and background effects with the APEX2 software program of Bruker AXS. The data were corrected for absorption using the multi-scan method (SADABS), leading to a significant improvement in R_{int} (merging residual value). No violation of $Fd\bar{3}m$ symmetry was noted.

Structure refinement was done with the SHELXL-2013 program (Sheldrick 2013). All reflections were used in the refinement. Variable parameters during the structural refinement were: overall scale factor, oxygen coordinate, site-scattering values, atomic-displacement parameters, and extinction parameter. Setting the origin at $\bar{3}m$, the initial atomic positions for oxygen atoms were taken from Bosi et al. (2010). The T site was modeled with Mg vs. Fe and the M site with Al (except for crystal $MgAl_2O_4$, which was modeled considering only ^{T}Mg and ^{M}Al because of being Fe free). Convergence was attained when the shifts in all refined parameters were less than their estimated standard deviation. Table 1 summarizes the structural parameters and refinement details.

Electron microprobe analysis and cation partitioning

The same crystals used for Brillouin scattering measurements were mounted on a glass slide and polished for electron microprobe analysis on a Cameca SX50 instrument equipped with four wavelength-dispersive spectrometers (WDS mode) and operated at an accelerating potential of 15 kV and a sample current of 15 nA, with an incident beam diameter of about 1 μm. For each sample, we collected 7–20 point analysis. Standards used were synthetic $MgAl_2O_4$ spinel and corundum (for Al), Fe_3O_4 (for Fe) and MgO (for Mg). PAP computer program was applied for raw data reduction (Pouchou and Pichoir 1984). Atomic fractions were calculated on the basis of four oxygen atoms (atoms per formula unit, apfu). The results, given in Table 2, are well supported by the match between the number of electrons per formula unit derived from chemical and structural analysis.

The intersite cation distribution was obtained by minimizing the residuals between calculated and observed chemical-structural data according to the procedure of Lavina et al. (2002). Optimized cation distributions are reported in Table 3.

Brillouin scattering measurements and data reduction

Brillouin scattering measurements were performed in the Brillouin Laboratory at GFZ German Research Centre for Geosciences in Potsdam, Germany. During the Brillouin scattering measurements, the samples were loaded into a sample holder obtained by sandwiching a 250 mm thick, face parallel, stainless steel disk (with a 2 mm diameter drilled chamber) between two diamond disks. The sample platelets were placed inside the sample chamber in contact with one of the two diamond plates. We found this system to be very useful for ambient condition measurements for two main reasons: (1) the sample can be quickly and easily removed from the holder and (2) diamond has a very high thermal conductivity, which allows to efficiently dissipate heat potentially produced by light absorption in the sample. We used a forward symmetric scattering geometry (e.g., Whitfield et al. 1976) and an external incidence angle of 60°. The mirror distance in the interferometer was 6 mm. We used a Verdi V2 solid state Nd:YVO_4 laser with a power at the sample of about 100 mW. To change systematically the orientation of the sample, the platelets were rotated along a horizontal axis starting from an arbitrary orientation in an angular range of 180° collecting a spectrum every 10°. The total number of probed velocities ranges between 31 and 48. The collection time for each spectrum was in the order of 1–2 h. Since iron tends to increase the absorption of light in our crystals (they

Table 1 Selected X-ray diffraction data for the spinels in the $(Mg,Fe)Al_2O_4$ series studied

Crystal	$MgAl_2O_4$	He2d	He2f	He3a	He5a	He6a
Crystal sizes (mm)	0.15×0.19×0.2	0.09×0.13×0.14	0.06×0.23×0.24	0.09×0.16×0.26	0.04×0.30×0.35	0.06×0.28×0.30
a (Å)	8.0853(4)	8.0886(4)	8.0926(2)	8.0951(3)	8.1137(2)	8.1217(3)
u	0.26200(5)	0.26203(4)	0.26223(3)	0.26201(4)	0.26277(4)	0.26299(4)
T-O (Å)	1.9185(7)	1.9197(5)	1.9235(5)	1.9210(6)	1.9362(5)	1.9411(6)
M-O (Å)	1.9292(4)	1.9298(3)	1.9293(3)	1.9315(3)	1.9304(3)	1.9307(3)
T-m.a.n	12.27(8)	12.48(5)	13.28(5)	14.27(6)	17.21(7)	18.38(7)
M-m.a.n	12.94(4)	12.88(3)	12.83(3)	13.21(4)	13.10(4)	13.22(4)
$T\text{-}U^{11}$ (Å^2)	0.0045(2)	0.00443(11)	0.00420(10)	0.00578(14)	0.00675(9)	0.00692(9)
$M\text{-}U^{11}$ (Å^2)	0.0046(1)	0.00449(8)	0.00456(8)	0.00475(11)	0.00505(8)	0.00514(9)
$M\text{-}U^{12}$ (Å^2)	–0.00014(4)	–0.00017(4)	− 0.00018(4)	− 0.00017(4)	− 0.00025(4)	− 0.00031(5)
$O\text{-}U^{11}$ (Å^2)	0.0078(1)	0.00757(10)	0.00781(9)	0.00761(11)	0.00027(8)	0.00906(12)
$O\text{-}U^{12}$ (Å^2)	0.00022(8)	0.00021(7)	0.00025(7)	0.00039(8)	0.00027(8)	0.00022(9)
Reciprocal range *hkl*	$-16 \le h \le 16$	$-13 \le h \le 14$	$-16 \le h \le 11$	$-16 \le h \le 13$	$-13 \le h \le 15$	$-16 \le h \le 13$
	$-13 \le k \le 15$	$-16 \le k \le 12$	$-13 \le k \le 16$	$-12 \le k \le 16$	$-15 \le k \le 15$	$-16 \le k \le 11$
	$-10 \le l \le 16$	$-13 \le l \le 12$	$-16 \le l \le 12$	$-16 \le l \le 12$	$-15 \le l \le 12$	$-11 \le l \le 16$
Total reflections	2410	2572	2465	2476	2572	2500
Unique reflections	133	127	133	132	131	134
$R_{int.}$ (%)	2.31	1.99	1.20	1.61	1.57	1.97
EXTI	0.173(8)	0.057(2)	0.0154(9)	0.0135(12)	0.0201(6)	0.0095(7)
*R*1 (%) all reflections	1.79	0.99	1.00	1.22	1.02	1.10
*wR*2 (%)	4.17	2.43	2.54	3.32	2.02	2.48
Goof	1.223	1.265	1.201	1.125	1.204	1.166
Diff. peaks ($\pm e$/Å^3)	– 0.44; 0.43	– 0.22; 0.19	– 0.21; 0.17	– 0.27; 0.25	– 0.29; 0.24	– 0.29; 0.27

Radiation, Mo–$K\alpha$ = 0.71073 Å. Data collection temperature = 293 K. Range for data collection $8° < 2\theta < 91°$. Origin fixed at $\bar{3}m$. Space group $Fd\bar{3}m$. $Z = 8$ formula units. Spinel structure has cations at Wyckoff positions $8a \equiv T$ (1/8, 1/8, 1/8) and $16d \equiv M$ (1/2, 1/2, 1/2), and oxygen anions at 32*e* (*u, u, u*)

a unit cell parameter, *u* oxygen fractional coordinate, *T*-O and *M*-O tetrahedral and octahedral bond lengths, respectively, *T*- and *M*-m.a.n., *T*- and *M*-mean atomic number, U^{11} atomic displacement parameter, $U^{11} = U^{22} = U^{33}$ and $U^{12} = U^{13} = U^{23}$ (=0 for *T*-site due to symmetry reasons); *EXTI* extinction parameter, $R_{int.}$ merging residual value, *R1* discrepancy index, calculated from *F*-data, *wR*2 weighted discrepancy index, calculated from F^2-data, *GooF* goodness of fit, *Diff. peaks* maximum and minimum residual electron density

Table 2 Chemical composition of the investigated Fe–Mg spinel samples

	$MgAl_2O_4$[a]	He2d	He2f	He3a	He5a	He6a
MgO (wt%)	28.5 (30)	27.37 (17)	25.89 (25)	22.06 (12)	17.19 (15)	13.51 (26)
Al_2O_3	71.0 (30)	71.56 (22)	71.19 (21)	67.54 (81)	63.06 (73)	64.13 (22)
FeO_{tot}	N/A	1.06 (4)	3.85 (40)	10.13 (12)	18.46 (22)	23.29 (39)
FeO[b]	N/A	N/A	3.78 (39)	9.73 (11)	17.72 (21)	22.12 (37)
Fe_2O_3[b]	N/A	N/A	0.09 (1)	0.45 (1)	0.82 (1)	1.29 (2)
Total	99.50 (4)	99.99 (28)	100.95 (51)	99.78 (83)	98.79 (77)	101.05 (50)
Atoms per formula units calculated on the basis of 4 oxygen atoms						
Mg	1.011 (6)	0.970 (5)	0.920 (7)	0.817 (7)	0.670 (5)	0.525 (9)
Al	1.992 (4)	2.006 (3)	2.001 (1)	1.978 (6)	1.945 (7)	1.970 (4)
Fe^{2+}	N/A	0.021 (1)	0.075 (8)	0.202 (3)	0.388 (7)	0.482 (8)
Fe^{3+}	N/A	0.000	0.001 (1)	0.008 (1)	0.016 (1)	0.025 (1)
Total cations	3.003	2.997(6)	2.999 (11)	3.007 (10)	3.019 (27)	3.002 (13)

Data from electron microprobe (7–20 point analyses), numbers in parenthesis are standard deviations for oxides and standard error (1σ, calculated by error propagation theory) for cations

[a]From Andreozzi et al. (2000)

[b]From Fe^{3+}/Fe_{Tot} ratios measured by Mössbauer spectroscopy (Halenius et al. 2002)

Table 3 Calculated cation site population in the investigated Fe–Mg samples

Cation	$MgAl_2O_4$	He2d	He2f	He3a	He5a	He6a
T-site						
Mg (apfu)	0.76	0.74	0.69	0.56	0.44	0.36
Fe^{2+}	0.00	0.02	0.08	0.17	0.33	0.42
Fe^{3+}	0.00	0.00	0.00	0.01	0.03	0.03
Al	0.24	0.24	0.23	0.26	0.20	0.19
Sum	1.00	1.00	1.00	1.00	1.00	1.00
M-site						
Mg	0.24	0.24	0.23	0.26	0.21	0.16
Fe^{2+}	0.00	0.01	0.01	0.03	0.03	0.07
Al	1.76	1.75	1.76	1.71	1.76	1.77
Sum	2.00	2.00	2.00	2.00	2.00	2.00

Cations expressed as atoms per formula unit (apfu)

become more opaque with increasing iron content), we reduced the incident laser intensity to avoid overheating of the sample and hence any possible Fe^{2+} oxidation and associated defects. As a consequence, the collection time for iron-rich samples (He5a and He6a) was significantly longer (2–3 h). Since the investigated materials become opaque for high iron content, we could not analyze crystals with $Fe^{2+} > 0.5$ apfu.

In a typical Brillouin scattering measurement, a beam of coherent light is shone into the sample to be investigated. A very small fraction of the scattered radiation is found to be frequency shifted with respect to the incident beam (Cummins and Schoen 1972; Grimsditch 2001). The frequency shift ($\Delta\omega$) is proportional to the speed of sound (v) in the probed direction, according to Whitfield et al. (1976):

$$v = \frac{\Delta\omega\lambda_0}{2\sin\theta_{ext}}. \quad (1)$$

In Eq. (1), λ_0 is the wavelength of the laser and θ_{ext} is the external angle of incidence in symmetric scattering geometry. In elastically anisotropic materials (like the vast majority of crystalline compounds including those belonging to the cubic system), the velocity and the polarization of an acoustic wave may change as a function of crystallographic direction. By measuring the velocities in two or more directions, it is possible to retrieve the full set of elastic constants (Every 1980; Newnham 2005).

Spinels crystallize in the cubic system (space group $Fd\bar{3}m$) and their elastic tensor is fully described by only three stiffness coefficients: C_{11}, C_{12} and C_{44} (in Voigt contracted index notation).

The full elastic tensors and the crystallographic orientations of the sample platelets were refined by performing a non-linear least-square fit of the set of Christoffel's equations corresponding to probed acoustic waves (Every 1980; Shimizu 1995). Uncertainties on the retrieved C_{ij} depends on errors associated with measured velocities, which in turn depend on uncertainties associated with peak position determination (frequency shift). The last step was to convert the single-crystal stiffnesses into an ideal isotropic polycrystalline bulk modulus (K_{S0}) and shear modulus (G_{VRH}) values using the Voigt–Reuss–Hill (VRH) averaging scheme (Eq. 2–5; Watt et al. 1976):

$$K_{S0} = K_V = K_R = \frac{(C_{11} + 2C_{12})}{3}, \quad (2)$$

$$G_{VRH} = \frac{G_V + G_R}{2}, \quad (3)$$

where

$$G_V = \frac{(C_{11} - C_{12} + 3C_{44})}{5}, \quad (4)$$

$$G_R = \frac{5(C_{11} - C_{12})C_{44}}{4C_{44} + 3(C_{11} - C_{12})}. \quad (5)$$

The subscripts "V" and "R" refer to the Voigt and Reuss bound values.

Results

Crystal chemistry

The results of the single-crystal X-ray diffraction measurements are reported in Table 1 and shown in Fig. 1. All the parameters increase linearly with increasing Fe content. As already noted by Andreozzi and Lucchesi (2002), the cation–oxygen distances in tetrahedra (*T*-O) increase at a much higher rate than cation–oxygen distances in octahedra

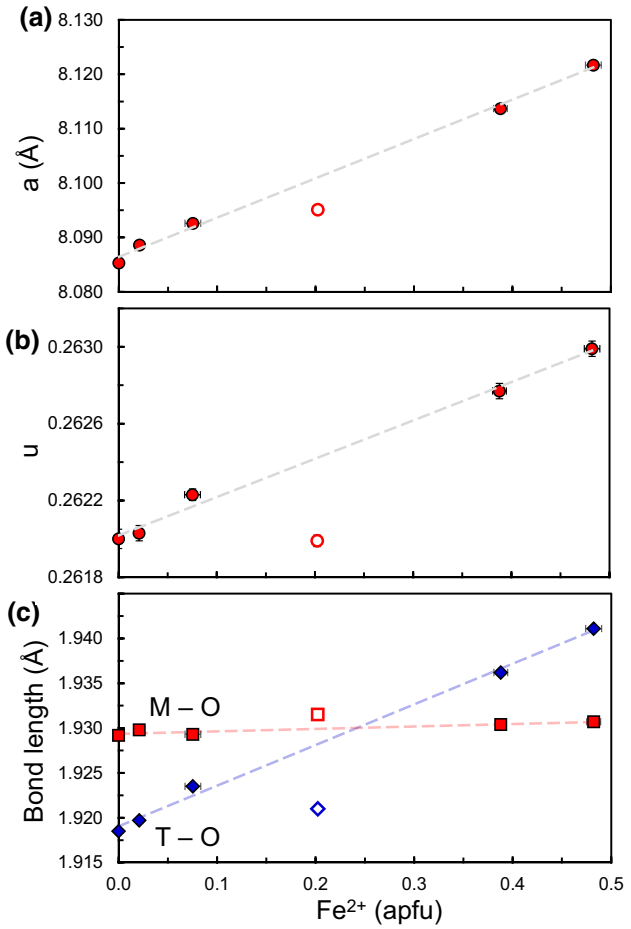

Fig. 1 The main crystallographic parameters plotted against Fe^{2+} content for the investigated Fe–Mg spinel samples: **a** unit cell parameter (*a*); **b** oxygen positional parameter (*u*); **c** cation–oxygen bond length in tetrahedra (*T*-O) and octahedra (*M*-O). Blue diamond symbols are for *T*-O, while red square symbols are for *M*-O. The open symbol represents sample He3a (see text for "Discussion"). Error bars are sometimes smaller than symbol size. Dashed lines are guides to the eye

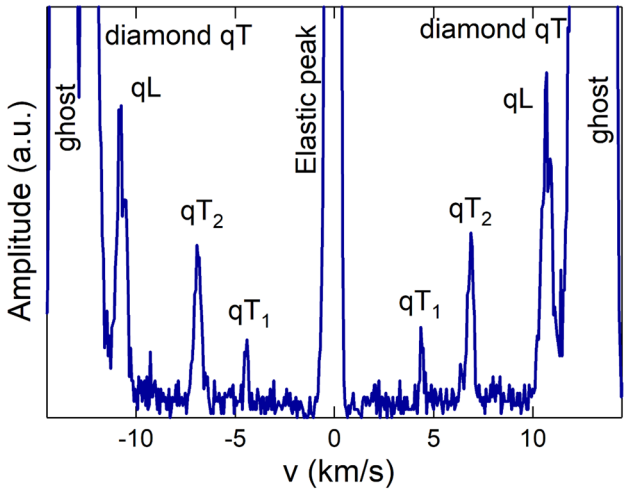

Fig. 2 Typical Brillouin spectrum. *qL* quasi-longitudinal wave, qT_2 and qT_1 quasi-transverse waves (fast and slow, respectively). The central peak corresponds to the unshifted radiation (Rayleigh scattering). At the far ends of the image, there are the qT wave of diamond and higher-order repetition of the central line (ghost). Intensity in arbitrary units (a.u.)

(*M*-O); therefore, the increase of the unit cell can be mainly attributed to the expansion of tetrahedra. In iron-poor compositions, *T*-O are shorter than *M*-O, while for iron-rich compositions the opposite is true. At about 0.20–0.25 Fe^{2+} apfu, *T*-O and *M*-O are expected to have the same value (Fig. 1c).

The chemical composition of the investigated $(Mg_{1-x},Fe_x)Al_2O_4$ spinel crystals is summarized in Table 2. The Fe^{2+} content progressively increases up to 0.48 apfu substituting for Mg, while Al content keeps almost stoichiometric with a minor substitution by Fe^{3+} at the highest Fe_{tot} contents. Most of the Fe^{2+} is found in tetrahedral coordination, with only a little fraction (reaching a maximum value of 0.07 apfu in He6a) hosted in the octahedra (Table 3). The very small amount of Fe^{3+} is found in tetrahedra. The tetrahedrally coordinated Al (which summed with the tetrahedrally coordinated Fe^{3+} corresponds to the inversion degree) decreases slightly but steadily along the investigated range, while the amounts in the octahedra remain constant. Overall, we can state that the increase of Fe^{2+}, which substitutes Mg in tetrahedra, is mainly responsible for the crystallographic variations observed in the $MgAl_2O_4$–$FeAl_2O_4$ solid solution. The results described here are in agreement with those reported in Andreozzi and Lucchesi (2002) for crystals grown in the same experimental batches, with the only important exception of sample He3a ($x = 0.202$) for which the structural parameters are significantly lower than expected (Table 1; Fig. 1).

Elasticity

In many spectra, we observed the longitudinal and both shear wave peaks (Fig. 2). The peak positions (that is the frequency shifts) were determined by least-square fits to pseudo-Voigt functions and velocities were calculated with Eq. (1). Fitted velocities are plotted in Fig. 3. The peaks in the spectra were fitted with a mixed Gaussian–Lorentian model. The R^2 coefficient ranged between 0.8 and 0.9.

The $C_{ij}s$ determined for the $(Mg,Fe^{2+})Al_2O_4$ series are reported in Table 4 along with the Fe^{2+} content, density, calculated from measured composition and unit cell volume, aggregate (isentropic) bulk and shear modulus and Zener anisotropy factor. The values of $C_{ij}s$ and elastic moduli are plotted against the Fe^{2+} content in Figs. 4 and 5, respectively. For low Fe^{2+} content (≤ 0.202 apfu), the stiffness tensor components C_{11} and C_{44} are almost

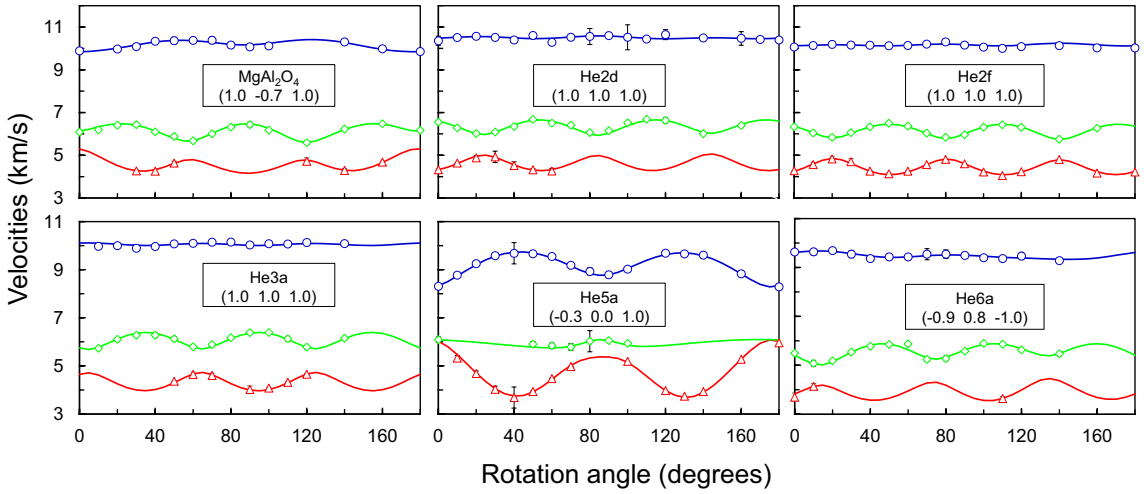

Fig. 3 Velocities measured as a function of rotation angle starting from an arbitrary direction. Blue circles are for quasi-longitudinal waves, green diamonds are for fast quasi-transverse waves and, red triangles are for slow quasi-transverse waves. The names of the samples and the crystallographic orientation of the platelets are shown at the center of each plot

Table 4 Density, Fe^{2+} content and elastic parameters of the investigated Fe–Mg samples

Sample	Density (g/cm^3)	Fe^{2+} (apfu)	C_{11} (GPa)	C_{12} (GPa)	C_{44} (GPa)	K_{S0} (GPa)	G_{VRH} (GPa)	A
$MgAl_2O_4$	3.57	0.000	282 (4)	156 (3)	154 (1)	198 (2)	108 (1)	2.44 (9)
He2d	3.59	0.021 (1)	282 (3)	161 (3)	154 (1)	201 (2)	106 (1)	2.55 (9)
He2f	3.63	0.075 (8)	281 (1)	160 (1)	151.2 (5)	200.4 (7)	104.7 (4)	2.50 (3)
He3a	3.72	0.202 (3)	279 (2)	162 (2)	152 (1)	201 (1)	103.7 (8)	2.60 (7)
He5a	3.84	0.388 (7)	263 (1)	163 (1)	142.6 (8)	196.4 (7)	93.7 (5)	2.85 (4)
He6a	3.92	0.482 (8)	263 (2)	165 (2)	135.8 (8)	197 (1)	90.3 (8)	2.77 (8)

Numbers between parentheses are calculated uncertainties (1σ, in the last digit). Typical uncertainties for density are in the order of 10^{-2} g/cm^3

K_{S0} isentropic bulk modulus, G_{VRH} Voigt–Reuss–Hill aggregate shear modulus, A Zener anisotropy factor ($2C_{44}/(C_{11}–C_{12})$)

constant. However, for $Fe^{2+}/(Mg + Fe^{2+})$ passing from 0.202 to 0.388, both parameters visibly decrease (− 7 and − 13%, respectively). Conversely the component C_{12} shows a linear trend characterized by a fairly small increase (5%) along the investigated compositional range (Fig. 4).

In cubic crystals, the bulk modulus (K_S) and the shear modulus (G) are defined by Eqs. (2) and (3–5), respectively. For the studied samples, taking into account the errors associated with the measurements (in average 1–2 GPa), K_S is poorly sensitive to chemical substitutions and only shows a weak negative trend with increasing Fe content (Fig. 5). On the contrary, G shows a large decrease (− 20%) along the investigated compositional range (Fig. 5). We have evaluated the elastic anisotropy quantified here by the Zener anisotropy ratio A ($A = 2C_{44}/(C_{11} - C_{12})$), which shows a linear increase of 13.5% across the investigated Fe range (Table 4).

Discussion

Our results for the elasticity of $MgAl_2O_4$ are completely consistent with literature data (Duan et al. 2018; Speziale et al. 2016; Fan et al. 2015; Suzuki et al. 2000; Askarpour et al. 1993; Yoneda 1990). However, in spite of the very simple chemistry of $MgAl_2O_4$ spinels, it is possible to observe some degree of scattering of the elastic moduli around the mean values corresponding to: $C_{11} = 284$ (2) GPa; $C_{12} = 155$ (1) GPa; $C_{44} = 154$ (1) GPa; $K_S = 198$ (1) GPa and $G = 108.4$ (7) GPa (Figs. 4, 5). Given the different synthesis processes used to produce the crystals discussed in this comparison (flux growth, flame fusion, Czochralski), it is highly possible that the different samples may be characterized by a different defect structure and/or non-stoichiometry, which in turn could affect the elastic response (e.g., Verma 1960; Schreiber 1967).

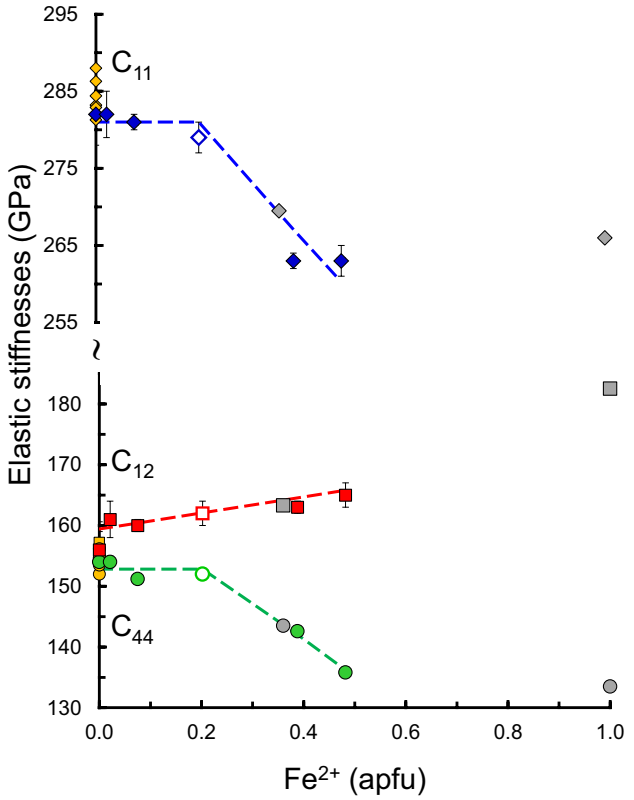

Fig. 4 Elastic stiffnesses (C_{ij}s) as a function of Fe^{2+} content for the Fe–Mg aluminate spinel samples. Diamonds are for C_{11}, squares are for C_{12} and circles for C_{44}. Open symbols represent sample He3a (see text for "Discussion"), while gray symbols are from Wang and Simmons (1972). Yellow symbols are for $MgAl_2O_4$ literature data (Yoneda 1990; Askarpour et al. 1993; Suzuki et al. 2000; Fan et al. 2015; Speziale et al. 2016; Duan et al. 2018). Dashed lines are guides to the eye. Error bars are sometimes smaller than symbol size

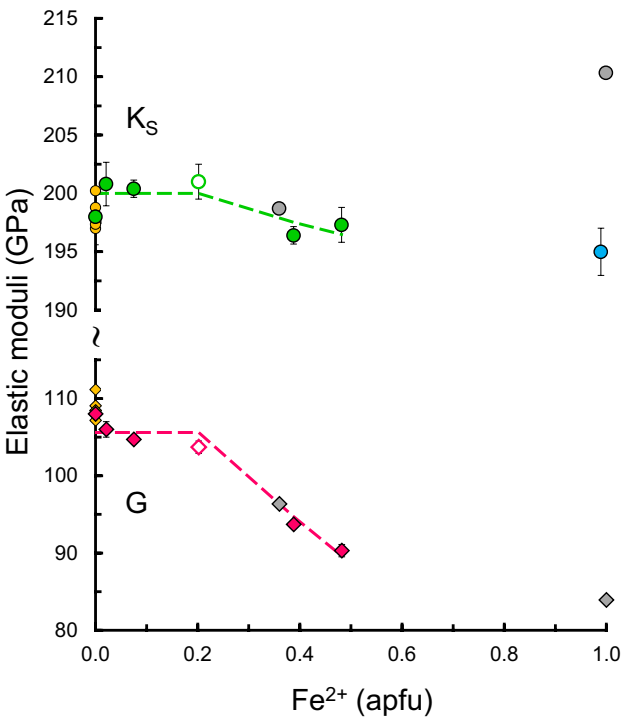

Fig. 5 Isentropic bulk modulus (K_S) and shear modulus (G_{VRH}) as a function of Fe^{2+} content for the Fe–Mg aluminate spinel samples. Circles are for Ks, while diamonds are for G_{VRH}. Gray symbols represent data from Wang and Simmons (1972), while turquoise symbol is for data from Nestola et al. (2015) corrected for the isentropic value. Open symbols represent sample He3a (see text for "Discussion"). Yellow symbols are for $MgAl_2O_4$ literature data (Yoneda 1990; Askarpour et al. 1993; Suzuki et al. 2000; Fan et al. 2015; Speziale et al. 2016; Duan et al. 2018). Dashed lines are guides to the eye. Error bars are sometimes smaller than symbol size

The observed deviation of the crystallographic parameters for sample He3a from the trend defined by the other crystals (see Fig. 1) is due to an anomalously high inversion degree (i.e., Al at the T site, see Table 3). In normal spinels, high values of inversion degree correspond to high cation disorder induced by high temperature, as demonstrated by Andreozzi et al. (2000), Andreozzi and Princivalle (2002) and Martignago et al. (2006). The high closure temperature recorded by the He3a sample is likely ascribed to a very fast cooling path, probably experienced by this crystal because it grew close to the walls of the crucible, whereas most of the other crystals grew in the central part of the crucible. In spite of that, we decided to leave sample He3a in the present dataset, because it represents an interesting opportunity to see if and how the cation disorder affects the elastic parameters. Our results show that the elastic parameters of sample He3a agree with the trend defined by the very Fe-poor samples (Figs. 4, 5). Even though there is not a general consensus on the role of cation distribution on the elastic properties of spinels (e.g., Askarpour et al. 1993; Hazen and Yang 1999; Li et al. 2007; Nestola et al. 2007), our data suggest that in the low-Fe portion of the series, spinel–hercynite ($0 \leq Fe^{2+} \leq 0.2$ apfu), cation disorder has minor effects on the elastic moduli (Figs. 4, 5).

The elasticity of iron aluminate spinels was studied by Wang and Simmons (1972) using ultrasounds interferometry on two samples, a natural one with composition $Mg_{0.75}Fe_{0.36}Al_{1.90}O_4$ and a synthetic one corresponding to the endmember hercynite $FeAl_2O_4$. In addition, Nestola et al. (2015) studied by high-pressure single-crystal X-ray diffraction a sample of $FeAl_2O_4$ synthesized in the same laboratory and under the same experimental conditions of the crystals investigated in this work. To obtain a consistent dataset, we converted the value of the isothermal bulk modulus (K_{T0}) given in Nestola et al. (2015) for the hercynite endmember (193.9 ± 1.7 GPa) into the isentropic value (K_{S0}) using the thermodynamic identity (Poirier 2000):

$$K_{S0} = K_{T0}(1 + \alpha\gamma T), \quad (6)$$

where α is the coefficient of thermal expansion (15.6×10^{-6}/K; Fei 1995), γ is the Grüneisen parameter (1.21; Stixrude and Bertelloni 2005 and references therein) and T is the absolute temperature.

The results obtained by Wang and Simmons (1972) for the natural spinel ($Fe^{2+} = 0.36$ apfu) are in perfect agreement with our data, and the result from Nestola et al. (2015) for hercynite is consistent with the trend for K_{S0} defined by the available data (Figs. 4, 5). On the contrary, the results for $FeAl_2O_4$ crystal by Wang and Simmons (1972) differ significantly from the trend defined by our experimental dataset. Our results show that the components C_{11}, C_{44} and G_{VRH} after an initial plateau extending to $x=0.202$ decrease as the Fe/(Fe + Mg) increases (Figs. 4, 5). There are not currently any additional published data on the elasticity of Fe^{2+}-rich aluminate spinels, However, assuming that linear relations between C_{11}, C_{44}, G_{VRH}, K_S and Fe^{2+} content hold true in the compositional range $0.388 < Fe^{2+} < 1$ apfu, we expect a significantly lower value of these moduli for hercynite with respect to $MgAl_2O_4$. Moreover, K_{S0} value for the synthetic $FeAl_2O_4$ measured by Wang and Simmons (1972) is largely different (about 7%) from K_{S0} obtained converting the isothermal result by Nestola et al. (2015). Only the elastic stiffness C_{12} determined by Wang and Simmons (1972) for $FeAl_2O_4$ agrees qualitatively with all the available experimental datasets. Considering the trend defined by our data and the data from Wang and Simmons (1972) for the natural pleonaste sample, also the value of the shear modulus for $FeAl_2O_4$ proposed by the same authors seems higher than a simple extrapolation of the other available data.

It is likely that the measurements of Wang and Simmons (1972) on $FeAl_2O_4$ may suffer from large unaccounted systematic errors which have led to an overestimation of the C_{ij}s and hence the elastic moduli. In fact, as discussed by the same authors and later recapped by Nestola et al. (2015), the $FeAl_2O_4$ crystal used for the ultrasonic measurements was unusually small to provide accurate measurements. In more detail, if the ratio between the wavelength used in the experiment and the length of the sample is unusually large (i.e., if the crystal is too small with respect to the wavelength), the resulting velocities (and hence the $C_{ij}s$) could be overestimated. Furthermore, as stated by Wang and Simmons (1972), the measurements along the <100> direction were particularly challenging due to phasing effects. In fact, any problem in the determination of the velocities in the <100> direction would directly influence the estimation of both C_{11} and C_{44} according to the following equations (Newnham 2005):

$$V_P^{<100>} = \sqrt{\frac{C_{11}}{\rho}}, \tag{7}$$

$$V_{S1}^{<100>} = V_{S2}^{<100>} = \sqrt{\frac{C_{44}}{\rho}}. \tag{8}$$

According to Eq. (2), a high value of C_{11} would lead to a high value in K_{S0}. In addition, recent literature shows that bulk modulus in oxide spinels is known be only slightly influenced by chemical substitution (e.g., Finger et al. 1986; Recio et al. 2001; Nestola et al. 2010, 2014). On this basis, the results for the synthetic $FeAl_2O_4$ by Wang and Simmons (1972) seem to be biased and inconsistent with the trend based on our results and the other available published data.

Due to the high optical absorption of the Fe-rich compositions, our study does not cover the full spinel–hercynite solid solution series, and the available data do not allow us to give a comprehensive (exhaustive) account of the compositional dependence of the elastic tensor in this system. Additional experimental and theoretical work, especially regarding the Fe-rich compositions, is definitely needed. Nevertheless, we can already provide a first consistent picture of the effect of Fe–Mg substitution on the elastic properties in the system $MgAl_2O_4$–$FeAl_2O_4$.

Magnesium and iron have a very different electronic structure, with magnesium being an alkaline earth metal, while iron is a transition metal. The different electronic structure of the two elements has profound consequences on the metal–oxygen bond strength, with direct impact on the local structure, phonon spectrum and elastic properties including anisotropy. Fe^{2+} in tetrahedral coordination, unlike Mg^{2+}, gives rise to dynamic Jahn–Teller effect (Goodenough 1964; Slack et al. 1966; Taran and Langer 2001; Skogby and Hålenius 2003). While many studies discussed the effect of Jahn–Teller (JT) ions on the structural properties of spinels at both room and high pressure (e.g., Waskowska et al. 2001; Nakamura and Fuwa 2014; Kyono et al. 2015), there is much less knowledge on how the JT effect affects elasticity. Syono et al. (1971) and Ishikawa and Syono (1971) attributed the anomalously low value of the (C_{11}–C_{12}) and C_{44} modes in Fe_2TiO_4 ulvöspinel to the JT effect caused by Fe^{2+} in tetrahedral coordination ($^{T}Fe^{2+}$). Wang and Simmons (1972) observed that both $FeAl_2O_4$ and Fe_2TiO_4 have about the same molar concentration of $^{T}Fe^{2+}$, but since the elastic stiffness coefficients of hercynite are by far much larger than ulvöspinel, the anomalous elastic behavior in Fe_2TiO_4 must not be solely due to the JT effect. The JT effect may explain, at least in part, the general decreasing trend of the $MgAl_2O_4$–$FeAl_2O_4$ series, although more experimental data on systems characterized by JT active ions are definitely needed to address the problem.

The substantially different characters of Fe–O bonding with respect to Mg–O bonding produce a large and almost linear softening of the longitudinal and shear elastic stiffnesses in the MgO–FeO solid solution series (Jacobsen et al. 2002). An overall softening effect is also observed in the spinel–hercynite series. However, in this case the compositional dependence of the elastic coefficients C_{11} and C_{44} is non-linear. At low Fe^{2+} content, the values of both C_{11} and C_{44} are

nearly independent of composition, while at Fe^{2+} contents above 20% they decrease with increasing Fe^{2+} content. Such non-linearity can be interpreted as due to a transition from a low concentration regime where the individual Fe atoms are isolated to one in which they show a cooperative behavior. The threshold between the two regimes can be interpreted as a critical percolation probability p_c (Broadbent and Hammersley 1957; Sykes and Essam 1964; van den Marck 1997). In the spinel structure, the cations are arranged in a $MgCu_2$-type sublattice where each tetrahedral (*A*) atom is surrounded by 16 close neighbors, 4 *A* "tetrahedral" atoms and 12 *B* "octahedral" atoms at very similar (less than 5% different) distances from the central *A* atom; in addition, the *B* atoms are arranged in a corner-sharing tetrahedral lattice with 6 *B* close neighbors at a distance almost 20% shorter than the *A*–*A* and *A*–*B* ones (e.g., Berry and Raynor 1953). In spinel–hercynite, Fe^{2+} is distributed almost only in the *A* sites ($X_{Fe}^{2+} \approx X_{Fe}^{2+}{}_{(A)}$, where $X_{Fe}^{2+}{}_{(A)}$ is the fraction of Fe^{2+} in the *A* site) in the samples with less than 10% Fe^{2+}–Mg substitution (He2d, He2f). In this case, the site percolation threshold corresponds to that of the tetrahedral sublattice, which is a diamond lattice with $p_c = 0.429$ (van der Marck 1997). Samples He3a and He5a ($X_{Fe}^{2+} = 0.202$ and 0.388 respectively) have a small, but detectable fraction of Fe^{2+} ($X_{Fe}^{2+}{}_{(B)}$) in the octahedral sites (see Table 3), and this decreases the site percolation threshold because there are 12 more close neighbors available for each tetrahedral atom and there is a finite probability of close neighbors Fe^{2+} in the *B*–*B* sublattice (which has $p_c = 0.39$; Scholl and Binder 1980). The percolation thresholds for interactions between cations in both *A, B* and *AB* sublattices have been treated in studies concerning the magnetic properties of spinels (Fiorani and Viticoli 1979a; Fiorani et al. 1979b; Scholl and Binder 1980). Following the results of Scholl and Binder (1980), who limited their analysis to *AB* interlattice interaction, and the reasoning of Hubsch et al. (1978), who also considered interactions in the *A* and *B* sublattices, we expect that site percolation threshold in spinel–hercynite is reached when the Fe^{2+} content is smaller than 0.429 (that is, the threshold for the *A* sublattice) due to the larger connectivity of the combined sublattices interactions (Fig. 6). This value is close to that determined for sample He5a (see Table 3).

The expected compositional threshold is qualitatively compatible with the results of our experimental study, which unfortunately do not include compositions between $X_{Fe^{2+}}$ 0.202 and 0.388. The value of p_c seems to be overestimated, especially with respect to the compositional dependence of C_{44}, which shows a change of behavior already at values of Fe^{2+} close to 0.2 apfu, based on the intersection of linear fits to the values determined below $X_{Fe^{2+}} = 0.202$ and above $X_{Fe^{2+}} = 0.388$ (Fig. 4). We can speculate that the presence of a resolvable fraction of Fe^{3+} in the tetrahedral sites of samples He3a, He5a and He6a (Table 3) could be also partially

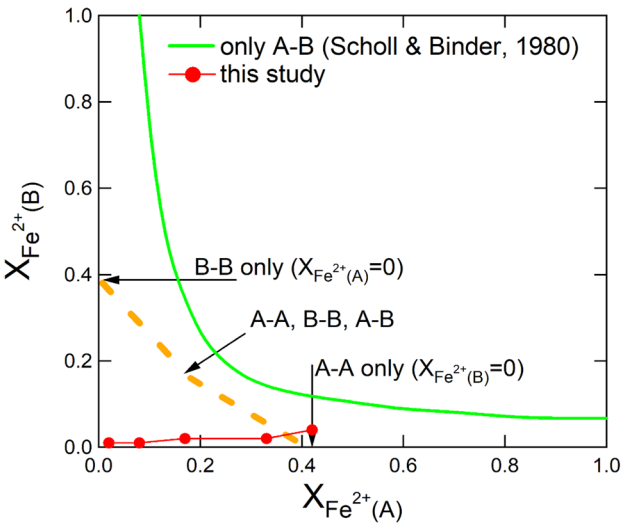

Fig. 6 Percolation threshold in the $X_{Fe^{2+}(B)} - X_{Fe^{2+}(A)}$ plane. The arrows indicate the threshold for the *A* and *B* sublattices (Fiorani and Viticoli 1979a; Fiorani et al. 1979b; Scholl and Binder 1980). The dashed orange line is a guide to the eye

responsible for the disagreement between our results and the value of p_c. In the $MgAl_2O_4$–$MnAl_2O_4$ solid solution series investigated by Bruschini et al. (2015), which does not contain resolvable amounts of Mn^{3+}, the strongest decrease of C_{11} and a visible decrease in C_{44} occur close to $Mn^{2+} = 0.47$ apfu. Notably, this value is quite similar to the estimated p_c of 0.429 for interactions only in the *A* sublattice.

Our results show a strong increase of the elastic anisotropy *A* with increasing Fe^{2+}. We compared our results with literature data on elastic anisotropy of other compounds containing Fe^{2+} and other transition metals (Mn^{2+} and Co^{2+}). In addition to spinels, the comparison was extended to NaCl-type (rock salt) structure compounds (MgO, MnO and CoO; Fig. 7 and electronic supplementary information), because this is a prototype structure adopted by important minerals of the Earth mantle, such as ferropericlase (Mg,Fe)O. Moreover, the cations Mg, Fe^{2+}, Mn^{2+} and Co^{2+} are mainly tetrahedrally coordinated in spinels, while they are octahedrally coordinated in the NaCl structure. Where data on endmember composition were only available, we assumed a linear dependency between the mole fraction of transition metal (X_M) and anisotropy. From this comparison, we highlighted several interesting points (Fig. 7): (1) the substitution of Fe^{2+} for Mg leads to opposite effects on the elastic anisotropy in (Mg,Fe)Al_2O_4 and (Mg,Fe)O. In spinels, we observe a linear increase of *A* as iron increases, whereas in (Mg,Fe)O the anisotropy exhibits a non-linear behavior, remaining constant in the range $0 < X_{Fe} < 0.25$ and then linearly decreasing for higher iron content (Jacobsen et al. 2002); (2) the values of the derivative $\partial A/\partial X_{Fe}^{2+}$ are identical (within uncertainties), but opposite in sign for spinel

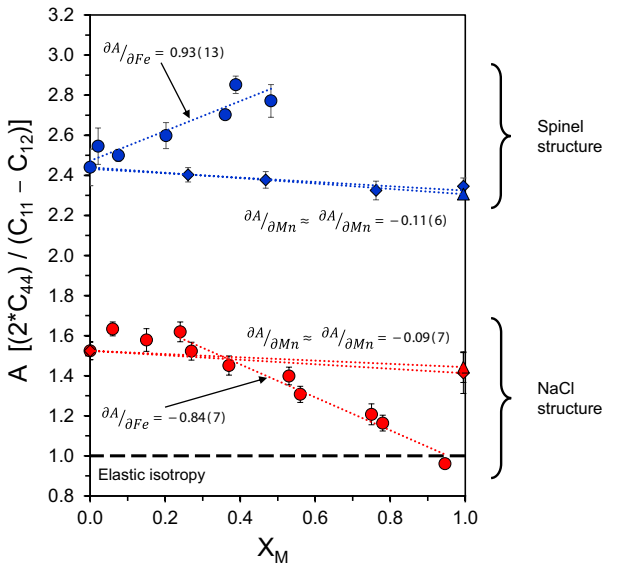

Fig. 7 Elastic anisotropy (Zener anisotropy factor A) for spinel structure (blue symbols) and rock salt structure (red symbols) binary compounds. Circles are for solid solution between Mg and Fe^{2+} aluminate endmembers. Diamonds are for solid solution between Mg and Mn^{2+} aluminate endmembers. Triangles are for solid solution between Mg and Co^{2+} aluminate endmembers. When data on endmembers were only available, a linear dependency of A against composition was assumed. Dotted lines are linear weighted fit of the data. $\partial A/\partial M$ indicates the slope of the fitted line. X_M denotes the mole fraction of the transition metal substituting for Mg. The value of $A = 1$, corresponding to elastic isotropy, is indicated by a dashed line. Data for Mg–Fe spinels: this study plus pleonaste from Wang and Simmons (1972); data for Mg–Mn spinels: Bruschini et al. (2015); data for Mg–Co spinels: Li et al. (1991); data for MgO–FeO: Jacobsen et al. 2002; data for MgO–MnO: average value from Webb et al. (1988), Uchida and Saito (1972), Sumino et al. (1980); data for MgO–CoO: average value form Uchida and Saito (1972), Sumino et al. (1980)

and rock salt structures (in rock salt structure, the derivative was calculated in the range $0.25 < X_{Fe} < 0.95$ being null for $0 < X_{Fe} < 0.25$; (3) an increase in Mn^{2+} and Co^{2+} causes a small decrease of the anisotropy in both spinel and rock salt structures; (4) the values of the derivative $\partial A/\partial X_{Mn^{2+}}$ and $\partial A/\partial X_{Co^{2+}}$ are identical (within uncertainties) in both spinels and rock salt structure: $\partial A/\partial X_{Mn^{2+}}{}^{\text{spinel}} = \partial A/\partial X_{Co^{2+}}{}^{\text{spinel}} = \partial A/\partial X_{Mn^{2+}}{}^{\text{rock salt}} = \partial A/\partial X_{Co^{2+}}{}^{\text{rock salt}}$.

Our results highlight the role of Fe^{2+} in determining the anisotropy of spinels, since it has a dramatic effect on elastic anisotropy with respect to other cations. It is interesting to note that the ionic radius of Fe^{2+} (0.63 Å) is intermediate between those of Mn^{2+} (0.66 Å) and Co^{2+} (0.58 Å; Shannon 1976), and hence elastic anisotropy can hardly be explained in terms of geometrical/crystallographic variations. It is possible that magnetic interactions between Fe atoms may contribute to the marked variation of the elastic anisotropy, although it is not clear why the anisotropy is enhanced in spinels and reduced in (Mg,Fe)O.

Conclusions

This work is the first systematic study which describes the elastic properties in the spinel ($MgAl_2O_4$)–hercynite ($FeAl_2O_4$) series. The Brillouin scattering measurements on synthetic crystals with $0 \le Fe^{2+} \le 0.5$ allowed us to elucidate the relationships between crystal chemistry and elastic properties. We showed that for low Fe^{2+} content ($Fe^{2+} \le 0.202$), the elastic properties remain unaltered, but for values of Fe/(Fe + Mg) equal or larger than 0.388 there is a general decrease of all parameters (with the exception of C_{12}). This behavior is explained according to the percolation theory and the transition between the low iron content region (constant parameters) and the high iron content region (linear decrease of the elastic moduli) occurs between 0.202 and 0.388 apfu of Fe^{2+}, which therefore corresponds to the critical percolation threshold (p_c). We also showed that cation disorder has very little or no influence on the elasticity of spinels with low Fe^{2+} content.

These results, especially if combined with additional data about the effect of pressure and temperature, will have direct implications in crustal and mantle petrology, as Fe^{2+}-bearing aluminate spinels are widespread accessory minerals in both the crust and the mantle, assuming also particularly high relevance as diamond inclusions (e.g., Nestola et al. 2015).

Acknowledgements We are very grateful to the two anonymous reviewers for their constructive comments which greatly improved our work and to C. McCammon for handling the manuscript. E.B. acknowledges support from Sapienza University of Rome ("Avvio alla ricerca 000047_13_GR_BRUSC"). G.B.A. acknowledges funding from "Progetto di ricerca Università 2015".

References

Andreozzi GB, Lucchesi S (2002) Intersite distribution of Fe^{2+} and Mg in the spinel (sensu stricto)—hercynite series by single crystal X-ray diffraction. Am Miner 87(8–9):1113–1120

Andreozzi GB, Princivalle F (2002) Kinetics of cation ordering in synthetic $MgAl_2O_4$ spinel. Am Miner 87(7):838–844

Andreozzi GB, Princivalle F, Skogby H, Della Giusta A (2000) Cation ordering and structural variations with temperature in $MgAl_2O_4$ spinel: an X-ray single-crystal study. Am Miner 85(9):1164–1171

Angel RJ (2000) Equations of state. Rev Miner Geochem 41(1):35–59

Angel RJ (2004) Equations of state of plagioclase feldspars. Contrib Miner Petrol 146(4):506–512

Angel RJ, Hazen RM, McCormick TC, Prewitt CT, Smyth JR (1988) Comparative compressibility of end-member feldspars. Phys Chem Miner 15(4):313–318

Askarpour V, Manghnani MH, Fassbender S, Yoneda A (1993) Elasticity of single-crystal $MgAl_2O_4$ spinel up to 1273 K by Brillouin spectroscopy. Phys Chem Miner 19(8):511–519

Bass JD, Sinogeikin SV, Li B (2008) Elastic properties of minerals: a key for understanding the composition and temperature of Earth's interior. Elements 4(3):165–170

Berry RL, Raynor GV (1953) The crystal chemistry of the Laves phases. Acta Crystallogr 6(2):178–186
Birch F (1938) The effect of pressure upon the elastic parameters of isotropic solids according to Murnaghan's theory of finite strain. J Appl Phys 9(4):279–288
Birch F (1947) Finite elastic strain of cubic crystals. Phys Rev 71(11):809
Birch F (1952) Elasticity and constitution of the Earth's interior. J Geophys Res 57(2):227–286
Birch F (1961) Composition of the Earth's mantle. Geophys J R Astron Soc 4:295
Bosi F, Hålenius U, Skogby H (2010) Crystal chemistry of the $MgAl_2O_4$–$MgMn_2O_4$–$MnMn_2O_4$ system: analysis of structural distortion in spinel-and hausmannite-type structures. Am Miner 95(4):602–607
Broadbent SR, Hammersley J (1957) Percolation processes: I. Crystals and mazes. In Math. Proc. Cambridge University Press, Cambridge. pp 629–641
Brown JM, McQueen RG (1986) Phase transitions, Grüneisen parameter, and elasticity for shocked iron between 77 GPa and 400 GPa. J Geophys Res Sol Earth 91:7485–7494
Bruschini E, Speziale S, Andreozzi GB, Bosi F, Hålenius U (2015) The elasticity of $MgAl_2O_4$–$MnAl_2O_4$ spinels by Brillouin scattering and an empirical approach for bulk modulus prediction. Am Miner 100(2–3):644–651
Buchen J, Marquardt H, Ballaran TB, Kawazoe T, McCammon C (2017) The equation of state of wadsleyite solid solutions: constraining the effects of anisotropy and crystal chemistry. Am Miner 102(12):2494–2504
Cummins HZ, Schoen PE (1972) Linear scattering from thermal fluctuations. Laser Handb 2(S1031)
Davies GF, Dziewonski AM (1975) Homogeneity and constitution of the Earth's lower mantle and outer core. Phys Earth Planet Interior 10:336–343
Duan Y, Li X, Sun N, Ni H, Tkachev SN, Mao Z (2018) Single-crystal elasticity of $MgAl_2O_4$-spinel up to 10.9 GPa and 1000 K: implication for the velocity structure of the top upper mantle. Earth Planet Sci Lett 481:41–47
Duffy TS, Vaughan MT (1988) Elasticity of enstatite and its relationship to crystal structure. J Geophys Res Sol Earth 93:383–391
Duffy TS, Zha CS, Downs RT, Mao HK, Hemley RJ (1995) Elasticity of forsterite to 16 GPa and the composition of the upper mantle. Nature 378:170–173
Every AG (1980) General closed-form expressions for acoustic waves in elastically anisotropic solids. Phys Rev B 22:1746
Fan D, Mao Z, Yang J, Lin JF (2015) Determination of the full elastic tensor of single crystals using shear wave velocities by Brillouin spectroscopy. Am Miner 100(11–12):2590–2601
Fei Y (1995) Thermal expansion. In: Ahrens TJ (ed) Mineral physics and crystallography: a handbook of physical constants. American Geophysical Union, Washington DC, pp 29–44
Finger LW, Hazen RM, Hofmeister AM (1986) High-pressure crystal chemistry of spinel ($MgAl_2O_4$) and magnetite (Fe_3O_4): comparisons with silicate spinels. Phys Chem Miner 13:215–220
Fiorani D, Viticoli S (1979a) Experimental evidence of a critical concentration for the long-range magnetic order in the A-sublattice of spinels. Solid State Commun 29:239–241
Fiorani D, Gastaldi L, Lapiccirella A, Viticoli S (1979b) Monte Carlo simulation of percolative phenomena in the cationic B-sublattice of spinels. Solid State Commun 32:831–832
Galasso FS (2016). Structure and properties of inorganic solids: international series of monographs in solid state physics. vol 7. Elsevier, Oxford
Giri AK, Mitra GB (1986) Elastic constants of solid solutions of ionic compounds. J Phys D Appl Phys 19:L5
Goodenough JB (1964) Jahn–Teller distortions induced by tetrahedral-site Fe^{2+} ions. J Phys Chem Solids 25:151–160
Grimsditch M (2001) Brillouin scattering. In Levy, Stern, (eds), Handbook of elastic properties of solids, liquids and gases, vol 1. Academic Press, London
Hålenius U, Skogby H, Andreozzi GB (2002) Influence of cation distribution on the optical absorption spectra of Fe^{3+}-bearing spinel ss-hercynite crystals: evidence for electron transitions in $^{VI}Fe^{2+}$–$^{VI}Fe^{3+}$ clusters. Phys Chem Miner 29:319–330
Hazen R, Navrotsky A (1996) Effects of pressure on order–disorder reactions. Am Miner 81:1021–1035
Hazen RM, Yang H (1999) Effects of cation substitution and order-disorder on P-V-T equations of state of cubic spinels. Am Mineral 84(11–12):1956–1960
Hubsch J, Gavoile G, Bolfa J (1978) Percolation and magnetic order in diluted spinels. J Appl Phys 49:1363–1365
Isaak DG, Graham EK (1976) The elastic properties of an almandine-spessartine garnet and elasticity in the garnet solid solution series. J Geophys Res 81:2483–2489
Ishikawa Y, Syono Y (1971) Giant magnetostriction due to Jahn–Teller distortion in Fe_2TiO_4. Phys Rev Lett 26:1335
Jackson I (1983) Some geophysical constraints on the chemical composition of the Earth's lower mantle. Earth Planet Sci Lett 62:91–103
Jackson I (2000) The Earth's mantle: composition, structure, and evolution. Cambridge University Press, Cambridge
Jackson I, Rigden SM (1996) Analysis of PVT data: constraints on the thermoelastic properties of high-pressure minerals. Phys Earth Planet Inter 96:85–112
Jackson I, Liebermann RC, Ringwood AE (1978) The elastic properties of $(Mg_xFe_{1-x})O$ solid solutions. Phys Chem Miner 3:11–31
Jacobsen SD, Reichmann HJ, Spetzler HA, Mackwell SJ, Smyth JR, Angel RJ, McCammon CA (2002) Structure and elasticity of single-crystal (Mg,Fe)O and a new method of generating shear waves for gigahertz ultrasonic interferometry. Sol Earth J Geophys Res:107
Jiang F, Speziale S, Duffy TS (2004) Single-crystal elasticity of grossular-and almandine-rich garnets to 11 GPa by Brillouin scattering. J Geophys Res Sol Earth 109:B10
Karki BB, Stixrude L, Clark SJ, Warren MC, Ackland GJ, Crain J (1997) Structure and elasticity of MgO at high pressure. Am Miner 82:51–60
Kurnosov A, Marquardt H, Frost DJ, Ballaran TB, Ziberna L (2017) Evidence for a Fe^{3+}-rich pyrolitic lower mantle from (Al,Fe)-bearing bridgmanite elasticity data. Nature 543(7646):543
Kyono A, Gramsch SA, Nakamoto Y, Sakata M, Kato M, Tamura T, Yamanaka T (2015) High-pressure behavior of cuprospinel $CuFe_2O_4$: Influence of the Jahn–Teller effect on the spinel structure. Am Miner 100:1752–1761
Lavina B, Salviulo G, Della Giusta A (2002) Cation distribution and structure modelling of spinel solid solutions. Phys Chem Miner 29:10–18
Li B, Liebermann RC (2007) Indoor seismology by probing the Earth's interior by using sound velocity measurements at high pressures and temperatures. Proc Natl Acad Sci 104:9145–9150
Li B, Zhang J (2005) Pressure and temperature dependence of elastic wave velocity of $MgSiO_3$ perovskite and the composition of the lower mantle. Phys Earth Planet Inter 151:143–154
Li Z, Fisher ES, Liu JZ, Nevitt MV (1991) Single-crystal elastic constants of Co–Al and Co–Fe spinels. J Mater Sci 26(10):2621–2624
Li L, Carrez P, Weidner D (2007) Effect of cation ordering and pressure on spinel elasticity by ab initio simulation. Am Miner 92:174–178
Lin JF, Speziale S, Mao Z, Marquardt H (2013) Effects of the electronic spin transitions of iron in lower mantle minerals: implications

for deep mantle geophysics and geochemistry. Rev Geophys 51:244–275

Lu C, Mao Z, Lin JF, Zhuravlev KK, Tkachev SN, Prakapenka VB (2013) Elasticity of single-crystal iron-bearing pyrope up to 20 GPa and 750 K. Earth Planet Sci Lett 361:134–142

Mao Z, Fan D, Lin JF, Yang J, Tkachev SN, Zhuravlev K, Prakapenka VB (2015) Elasticity of single-crystal olivine at high pressures and temperatures. Earth Planet Sci Lett 426:204–215

Marquardt H, Speziale S, Jahn S, Ganschow S, Schilling FR (2009) Single-crystal elastic properties of $(Y,Yb)_3Al_5O_{12}$. J Appl Phys 106:3519

Martignago F, Andreozzi GB, Dal Negro A (2006) Thermodynamics and kinetics of cation ordering in natural and synthetic $Mg(Al,Fe^{3+})_2O_4$ spinels from in situ high-temperature X-ray diffraction. Am Miner 91:306–312

Mori-Sánchez P, Marqués M, Beltrán A, Jiang JZ, Gerward L, Recio JM (2003) Origin of the low compressibility in hard nitride spinels. Phys Rev B 68(6):064115

Murakami M, Ohishi Y, Hirao N, Hirose K (2012) A perovskitic lower mantle inferred from high-pressure, high-temperature sound velocity data. Nature 485(7396):90

Nakamura S, Fuwa A (2014) Local and dynamic Jahn–Teller distortion in ulvöspinel Fe_2TiO_4. Hyperfine Interact 226:267–274

Nestola F, Ballaran TB, Liebske C, Bruno M, Tribaudino M (2006) High-pressure behaviour along the jadeite $NaAlSi_2O_6$–aegirine $NaFeSi_2O_6$ solid solution up to 10 GPa. Phys Chem Miner 33:417–425

Nestola F, Boffa Ballaran T, Balic-Zunic T, Princivalle F, Secco L, Dal Negro A (2007) Comparative compressibility and structural behavior of spinel $MgAl_2O_4$ at high pressures: the independency on the degree of cation order. Am Miner 92:1838–1843

Nestola F, Ballaran TB, Koch-Müller M, Balic-Zunic T, Taran M, Olsen L, Princivalle F, Secco L, Lundegaard L (2010) New accurate compression data for γ-Fe_2SiO_4. Phys Earth Planet Inter 183:421–425

Nestola F, Periotto B, Andreozzi GB, Bruschini E, Bosi F (2014) Pressure–volume equation of state for chromite and magnesiochromite: a single-crystal X-ray diffraction investigation. Am Miner 99:1248–1253

Nestola F, Periotto B, Anzolini C, Andreozzi GB, Woodland AB, Lenaz D, Alvaro M, Princivalle F (2015) Equation of state of hercynite, $FeAl_2O_4$, and high-pressure systematics of Mg–Fe–Cr–Al spinels. Miner Mag 79:285–294

Newnham RE (2005) Properties of materials: anisotropy, symmetry, structure. Oxford University Press, Oxford

Pamato MG, Kurnosov A, Ballaran TB, Frost DJ, Ziberna L, Giannini M, Speziale S, Tkachev SN, Zhuravlev KK, Prakapenka VB (2016) Single crystal elasticity of majoritic garnets: stagnant slabs and thermal anomalies at the base of the transition zone. Earth Planet Sci Lett 451:114–124

Poirier JP (2000) Introduction to the physics of the Earth's interior, 2nd edn. Cambridge University Press, Cambridge

Pouchou JL, Pichoir F (1984) A new model for quantitative X-ray microanalysis. I. Application to the analysis of homogeneous samples. Rech Aerosp 3:167–192

Recio JM, Franco R, Pendás AM, Blanco MA, Pueyo L, Pandey R (2001) Theoretical explanation of the uniform compressibility behavior observed in oxide spinels. Phys Rev B 63:184101

Reichmann HJ, Jacobsen SD (2006) Sound velocities and elastic constants of $ZnAl_2O_4$ spinel and implications for spinel-elasticity systematics. Am Miner 91:1049–1054

Reichmann HJ, Jacobsen SD, Mackwell SJ, McCammon CA (2000) Sound wave velocities and elastic constants for magnesiowüstite using gigahertz interferometry. Geophys Res Lett 27:799–802

Reichmann HJ, Jacobsen SD, Boffa Ballaran T (2013) Elasticity of franklinite and trends for transition-metal oxide spinels. Am Miner 98:601–608

Scholl F, Binder K (1980) Selective sublattice dilution in ordered magnetic compounds: a new kind of percolation problem. Z Phys B Condens Matter 39:239–247

Schreiber E (1967) Elastic moduli of single-crystal spinel at 25 °C and to 2 kbar. J Appl Phys 38(6):2508–2511

Shannon RD (1976) Revised effective ionic radii and systematic studies of interatomic distances in halides and chalcogenides. Acta Crystallogr A 32(5):751–767

Sheldrick GM (2013) SHELXS 2013, program for crystal structure solution. University of Göttingen, Göttingen

Shimizu H (1995) High-pressure Brillouin scattering of molecular single-crystals grown in a diamond-anvil cell. In: Senoo M, Suito K, Kobayashi T, Kubota H (eds) High pressure research on solids. Elsevier, Amsterdam, pp 1–17

Sickafus KE, Wills JM, Grimes NW (1999) Structure of spinel. J Am Ceram Soc 82:3279–3292

Skogby H, Hålenius U (2003) An FTIR study of tetrahedrally coordinated ferrous iron in the spinel–hercynite solid solution. Am Miner 88:489–492

Slack GA, Ham FS, Chrenko RM (1966) Optical absorption of tetrahedral Fe^{2+}(3d6) in cubic ZnS, CdTe, and $MgAl_2O_4$. Phys Rev 152:376

Slagle OD, McKinstry HA (1967) Temperature dependence of the elastic constants of the alkali halides. I. NaCl, KCl, and KBr. J Appl Phys 38:437–446

Speziale S, Duffy TS, Angel RJ (2004) Single-crystal elasticity of fayalite to 12 GPa. J Geophys Res Sol Earth 109:B12

Speziale S, Nestola F, Jiang F, Duffy T (2016) Single-crystal elastic constants of spinel ($MgAl_2O_4$) to 11.1 GPa by Brillouin scattering. In: Abstract MR23A-2658 2016 Fall Meeting. AGU, San Francisco

Steinle-Neumann G, Stixrude L, Cohen RE, Gülseren O (2001) Elasticity of iron at the temperature of the Earth's inner core. Nature 413:57–60

Stixrude L, Lithgow-Bertelloni C (2005) Thermodynamics of mantle minerals—I. Physical properties. Geophys J Int 162:610–632

Sumino Y, Kumazawa M, Nishizawa O, Pluschkell W (1980) The elastic constants of single crystal $Fe_{1-x}O$, MnO and CoO, and the elasticity of stoichiometric magnesiowüstite. J Phys Earth 28(5):475–495

Suzuki I, Ohno I, Anderson O (2000) Harmonic and anharmonic properties of spinel $MgAl_2O_4$. Am Miner 85:304–311

Sykes MF, Essam JW (1964) Critical percolation probabilities by series methods. Phys Rev 133:A310

Syono Y, Fukai Y, Ishikawa Y (1971) Anomalous elastic properties of Fe_2TiO_4. J Phys Soc Jpn 31:471–476

Taran MN, Langer K (2001) Electronic absorption spectra of Fe^{2+} ions in oxygen-based rock-forming minerals at temperatures between 297 and 600 K. Phys Chem Miner 28:199–210

Tatli A, Özkan H (1987) Variation of the elastic constants of tourmaline with chemical composition. Phys Chem Miner 14:172–176

Uchida N, Saito S (1972) Elastic constants and acoustic absorption coefficients in MnO, CoO, and NiO single crystals at room temperature. J Acoust Soc Am 51(5B):1602–1605

van der Marck SC (1997) Percolation thresholds and universal formulas. Phys Rev Earth 55:1514

Verma RK (1960) Elasticity of some high-density crystals. J Geophys Res 65(2):757–766

Wang H, Simmons G (1972) Elasticity of some mantle crystal structures: 1. Pleonaste and hercynite spinel. J Geophys Res 77:4379–4392

Waskowska A, Gerward L, Olsen JS, Steenstrup S, Talik E (2001) $CuMn_2O_4$: properties and the high-pressure induced Jahn–Teller phase transition. J Phys Condens Matter 13:2549

Watt JP, Davies GF, O'Connell RJ (1976) The elastic properties of composite materials. Rev Geophys 14:541–563

Webb SL, Jackson I, Gerald JF (1988) High-pressure elasticity, shear-mode softening and polymorphism in MnO. Phys Earth Planet Interior 52(1–2):117–131

Whitfield CH, Brody EM, Bassett WA (1976) Elastic moduli of NaCl by Brillouin scattering at high pressure in a diamond anvil cell. Rev Sci Instrum 47:942–947

Yang J, Mao Z, Lin JF, Prakapenka VB (2014) Single-crystal elasticity of the deep-mantle magnesite at high pressure and temperature. Earth Planet Sci Lett 392:292–299

Yoneda A (1990) Pressure derivatives of elastic constants of single crystal MgO and $MgAl_2O_4$. J Phys Earth 38(1):19–55

Zhang JS, Bass JD (2016) Sound velocities of olivine at high pressures and temperatures and the composition of Earth's upper mantle. Geophys Res Lett 43(18):9611–9618

Zhang J, Reeder RJ (1999) Comparative compressibilities of calcite-structure carbonates: deviations from empirical relations. Am Miner 84:861–870